Nanoscale Advances

ROYAL SOCIETY OF CHEMISTRY

PAPER

View Article Online
View Journal | View Issue

Cite this: *Nanoscale Adv.*, 2021, **3**, 3279

Large piezoelectric and thermal expansion coefficients with negative Poisson's ratio in strain-modulated tellurene†

Parrydeep Kaur Sachdeva, [abc] Shuchi Gupta [b] and Chandan Bera *[a]

Received 6th November 2020
Accepted 6th April 2021

DOI: 10.1039/d0na00930j

rsc.li/nanoscale-advances

Two dimensional (2D) chalcogenide monolayers have diversified applications in optoelectronics, piezotronics, sensors and energy harvesting. The group-IV tellurene monolayer is one such emerging material in the 2D family owing to its piezoelectric, thermoelectric and optoelectronic properties. In this paper, the mechanical and piezoelectric properties of 2D tellurene in centrosymmetric β and non-centrosymmetric β′ phases are investigated using density functional theory. β′-Te has shown a negative Poisson's ratio of −0.024 along the zigzag direction. Giant in-plane piezoelectric coefficients of −83.89 × 10^{-10} C m^{-1} and −42.58 × 10^{-10} C m^{-1} are observed for β′-Te under biaxial and uniaxial strains, respectively. The predicted values are remarkably higher, that is 23 and 12 times the piezoelectric coefficient of a MoS_2 monolayer with biaxial and uniaxial strain in the zigzag direction, respectively. A large thermal expansion coefficient of tellurene is also estimated using quasi harmonic approximation. High piezoelectricity combined with exotic mechanical and thermal properties makes tellurene a very promising candidate in nanoelectronics.

1 Introduction

2D materials provide a great platform to investigate and exploit their properties for applications on a vast scale from space and defense to miniaturized energy conversion devices. Previous studies[1,2] have shown that materials in monolayer or 2D form exhibit novel properties that do not exist in their 3D forms. Piezoelectricity is one such property that is being studied extensively in 2D materials.[3–6] Most of the bulk crystals have a center of symmetry which subsequently is not found in their 2D structures. Due to the broken symmetry, the widely known MoS_2 [1,7,8] monolayer and its Janus structures such as MoSSe, MoSTe,[9] and MoSeTe[10] possess piezoelectricity. Other members of 2D transition metal dichalcogenides (TMDCs) exhibiting the piezoelectric effect include WS_2, WSe_2, WTe_2 and their Janus monolayers WSSe, WSTe, and WSeTe.[10] These have piezoelectric coefficients comparable to that of MoS_2. Group IV TMDCs[5] of type MX_2 (M = Zr and Hf, X = S, Se, and Te) do not belong to the class of piezoelectric materials due to the existence of inversion centrosymmetry in them. However, the derived Janus structures MXY (such as ZrSSe, HfSSe and so on) are staggered with broken inversion symmetry and display piezoelectric coefficients in the range higher than that of MoS_2. Besides dichalcogenides, monochalcogenides have also been investigated for this property. Li *et al.*[11] revealed the piezoelectricity of group-III monochalcogenides InSe, GaSe and GaSe to be of the same order as that of MoS_2. Large piezoelectricity has been observed in the monolayers of group-IV monochalcogenides GeS, GeSe, SnS and SnSe.[12,13] Furthermore, Blonsky *et al.*[2] have determined the in-plane coefficients for 37 piezoelectric materials that include 2D TMDCs (CrS_2, $NbSe_2$), metal oxides (ZnO, MgO) and III–V semiconductor materials (GaAs, BSb, *etc.*). Among 2D materials, another class called Mxenes has emerged owing to its potential in piezotronics. Tan *et al.*[14] reported huge piezoelectricity in the out-of-plane direction for an oxygen functionalized MXene, M_2CO_2. Zhang *et al.*[15] predicted three phases of ferroelectric Mxenes and reported the existence of piezoelectricity in M_2CS_2 and M_2CO_2. Piezoelectricity has been reported even in monoelemental materials such as black phosphorus (BP)[16,17] and α-Te.[18] BP has a piezoelectric coefficient of −9.48 pm V^{-1} which is comparable to that of TMDCs.[2] α-Te has small asymmetry in its structure which has been exploited to realize the out-of-plane piezoelectricity in it. Also, the piezotronic effect has been explored in 1D van der Waals Te nanobelts for their utilization in smart electronic devices.[19]

Another emergent characteristic observed in monoelemental 2D materials such as graphene[20] and phosphorene[21,22] is negative Poisson's ratio (NPR). In-plane NPR emerges in graphene while out-of-plane NPR exists in black phosphorus. The difference lies in the mechanism for the structural compensation of

[a]*Institute of Nano Science and Technology, Knowledge City, Sector-81, S. A. S Nagar, Mohali, Punjab 140306, India. E-mail: chandan@inst.ac.in*

[b]*University Institute of Engineering and Technology, Panjab University, Sector-25, Chandigarh 160014, India*

[c]*Department of Physics, Panjab University, Sector-14, Chandigarh 160014, India*

† Electronic supplementary information (ESI) available. See DOI: 10.1039/d0na00930j

the strain. NPR has been observed in a few 2D materials having honeycomb lattices such as silicene, h-BN, h-GaN, h-SiC, and h-BAs.[23] A few 2D heterostructures constructed with graphene/MoS_2 and graphene/h-BN[24] also show negative Poisson's ratio. Initially, the NPR behaviour was explored in systems such as crystalline SiO_2,[25] metallic nanoplates,[26] 2D isotropic systems[27] and chiral honeycomb systems.[28] These materials with a negative Poisson's ratio have many promising applications in defense, biomedical, *etc.*[21,29] Mechanical metamaterials have superior physical properties compared to conventional materials with a positive Poisson's ratio.

Preferable thermal properties when combined with their mechanical properties become very suitable for device applications. Among 2D chalcogenides, graphene displays negative thermal expansion in the temperature range 0–1000 K.[30,31] Doping graphene with nitrogen and boron makes the thermal expansion coefficient more negative. Negative thermal expansion is caused by the transverse acoustic modes present in graphene, which result in highly negative Grüneisen parameter. Simulations by Sevik[30] revealed that h-BN exhibits a high negative thermal expansion (-6.5×10^{-6} K^{-1}) compared to graphene (-3.6×10^{-6} K^{-1}). Huang *et al.*[32] reported negative to high positive variation of thermal expansion with temperature in MoS_2. A similar variation in thermal expansion has been observed for $MoTe_2$.[33] Another TMDC, 2H-WS_2 also shows negative thermal expansion up to 1100 K.[34] A negative volumetric expansion exists in GeTe depending upon the thermal evolution of its structure. Herein, the coupling of acoustic and soft transverse optical modes causes the negative thermal expansion.[35] Black phosphorus possesses anisotropic thermal expansion with negative values in the zigzag direction.[36]

Since the mechanical exfoliation of graphene,[37] researchers from all over the globe have come to terms with the possibility of extracting 2D materials from their bulk counterparts. Ultrathin Te films have already been synthesized using different approaches such as by extracting monolayers from layered bulk tellurium *via* the liquid-phase exfoliation method or by growing Te monolayers on a substrate using physical vapor deposition, epitaxial formation by molecular beam epitaxy and synthesis of free standing 2D Te by the solution method.[38–43] Wu *et al.*[44] constructed a 2D FET device with a large drain current of 300 mA mm^{-1}, high mobility and high on/off ratio. Te has superior transport properties that make it suitable for thermoelectric applications.[41,43,45,46] It has high carrier mobilities leading to good electrical conductivity and the heavy Te atoms result in flat bands towards the conduction region which increase the Seebeck coefficient.[47] The unusually low thermal conductivity in tellurene is a major contributing factor towards increasing its power factor and efficiency in a thermoelectric device.[48,49] Also, theoretical reports have shown that Te has a direct band gap,[50,51] and hence, optical to electrical energy can be harnessed from it.[41,42,52] Te is fundamentally centrosymmetric but becomes non-centrosymmetric upon strain engineering. Also, strain is an unavoidable entity during the fabrication of thin films. Nowadays, strain is also intentionally used to modulate the properties.

In this article, we have investigated the mechanical and piezoelectric properties of single layer tellurene under strain along with its temperature dependent expansion. The motivation of this work lies in a few previous reports indicating the origin of ferroelectricity and polarizations in monoelemental tellurene.[53,54] Two stable structures of 2D Te are obtained in this study; where one structure is centrosymmetric and the other one is non-centrosymmetric. Anomalous piezoelectric coefficients and Poisson's ratio are observed in the non-centrosymmetric 2D Te.

2 Computational methods

The structural optimization and the piezoelectric calculations of 2D tellurene have been done using density functional theory (DFT) as implemented in Vienna *Ab initio* Simulation Package (VASP),[55] with projector augmented waves (PAW)[56,57] in the generalized-gradient approximation (GGA).[58] The electron exchange and correlation effects are described using the Perdew–Burke–Ernzerhof (PBE)[59] functional. A vacuum of 15 Å along the *c*-direction is used to avoid the interaction between the periodic layers. The plane wave cutoff energy is set to 400 eV and the Brillouin zone is sampled with a $14 \times 14 \times 1$ gamma centered *k*-mesh. The atomic positions have been relaxed until the forces are less than 0.01 eV $Å^{-1}$. The energy convergence criterion for electronic relaxation is set at 10^{-8} eV to have energy values with higher accuracy. The piezoelectric coefficients and Born effective charges (BEC) are calculated using the density functional perturbation theory (DFPT).[60,61] The finite difference method[62] is used to calculate the elastic constants in VASP. The thermal expansion of tellurene is calculated with quasi-harmonic approximation (QHA) using Phonopy.[63] Phonon frequencies are obtained using the supercell approach with a $5 \times 4 \times 1$ supercell and a $3 \times 3 \times 1$ *k*-mesh using Phonopy.[64]

3 Results and discussion

Bulk tellurium belongs to the non-centrosymmetric trigonal space group $P3_121$ (152). Very small ($e_{11} = 1.19$ C m^{-2}) piezoelectricity is observed in it (ESI†). The single layer tellurene is a puckered structure consisting of alternate planar four-membered and chair-like six-membered rings as shown in Fig. 1(a). The arrangement of atoms is different as viewed along the *a* and *b*-axes, namely armchair and zigzag directions, respectively. The completely optimized tellurene has lattice constants $a = 5.69$ Å, $b = 4.22$ Å and $c = 4.12$ Å with the space group $P2/m$ (10). Zhu *et al.*[50] have reported similar lattice constants $a = 5.49$ Å and $b = 4.17$ Å for monolayer Te. The optimized non-centrosymmetric structure with lattice parameters $a = 5.96$ Å and $b = 4.51$ Å is obtained with the monoclinic space group $P2(3)$ from bulk Te exfoliation. Hereafter in this manuscript, the centrosymmetric structure with the space group $P2/m$ is called β and the non-centrosymmetric structure with the space group $P2$ is called β′. Inequivalent Te–Te bonds and the difference in their bond lengths (Fig. 1(a)) clearly show the absence of mirror planes in the β′ structure. In Fig. 1(a), numbers are provided to Te-atoms in the 2D sheet to

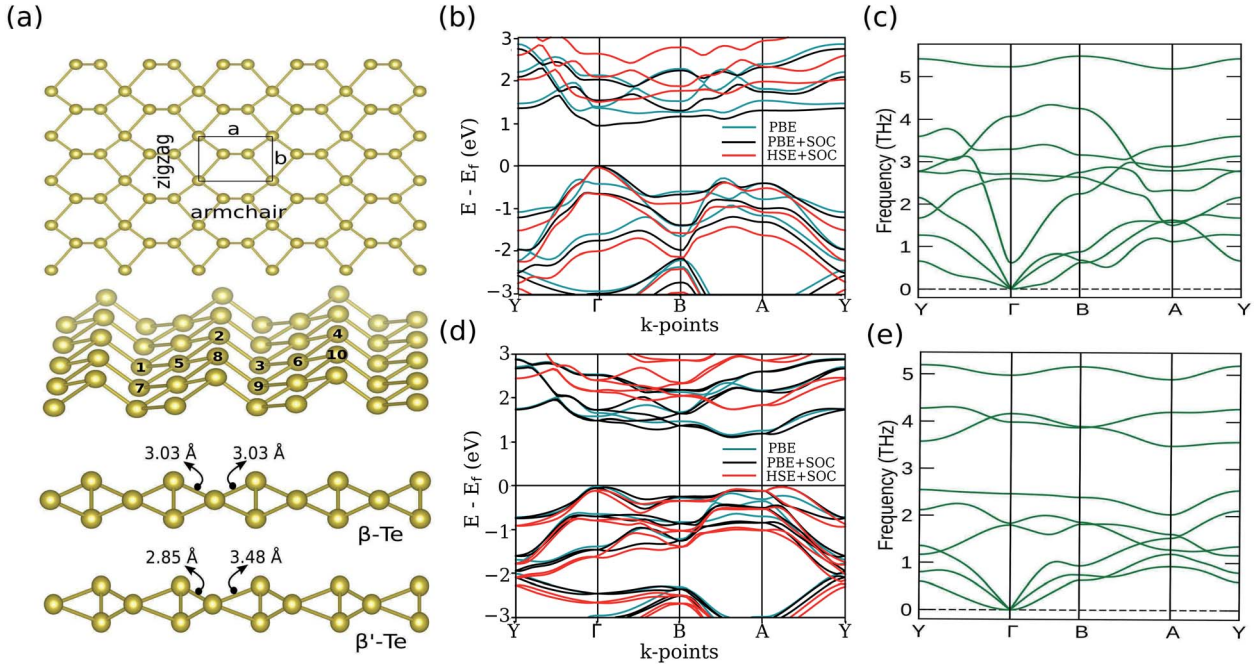

Fig. 1 (a) Geometric structure of monoclinic 2D tellurene: top view of the structure displaying the armchair and zigzag directions (unit cell is shown with a black box), the perspective view showing the puckered configuration of the structure (numbers on Te-atoms help in identifying and understanding their relative movements) and side views of β-Te and β′-Te highlighting the different bond lengths responsible for centrosymmetry and non-centrosymmetry in the monolayer. (b and d) Electronic band structures and (c and e) phonon band structures of the β and β′-tellurene monolayer, respectively.

understand the atom movements under strain that are discussed in the paper. The structural stability of the tellurene monolayer is investigated *via* phonon dispersion calculations. The phonon spectra of β-Te (Fig. 1(c)) and β′-Te (Fig. 1(e)) monolayers are found to be perfectly stable.

β-Te (Fig. 1(b)) shows an indirect 1.26 eV band gap in the Γ → BA direction with the PBE functional. The inclusion of spin–orbit coupling changes the band gap to 0.96 eV and makes it direct. The band gap calculated using the HSE functional is 1.81 eV and is indirect. In a similar manner, the incorporation of SOC makes the band gap direct and reduces it to 1.48 eV. The calculated band gaps for β-Te using different functionals are in reasonable agreement with previous theoretical reports.[50,52,65] On the other hand, the β′-Te monolayer (Fig. 1(d)) displays indirect band gaps of 1.18 eV and 1.13 eV with PBE and PBE + SOC, respectively. The HSE and HSE + SOC functionals also result in indirect band gaps of 1.89 eV and 1.74 eV, larger than the ones obtained using the PBE functional. The band structures obtained using HSE with and without spin–orbit coupling are shown explicitly in the ESI, Fig. S5.†

The mechanical strength of 2D structures to withstand strain can be measured by computing their Poisson's ratio. In the case of a monolayer, the in-plane Poisson's ratio is the most significant component. We investigated this quantity for single layer β-Te and β′-Te by deforming them uniaxially in the zigzag and armchair directions with the strain in the range of −10% to +10%. Once the structures get relaxed and optimized, energy–strain relations are obtained (ESI, Fig. S1 and S2†).

Poisson's ratio is computed as $\nu = -\frac{\partial \varepsilon_a}{\partial \varepsilon_b}\left(\text{or } -\frac{\partial \varepsilon_b}{\partial \varepsilon_a}\right)$, where ε_a is the strain generated along the *a*-axis in response to the applied strain εb along the *b*-axis or *vice versa*. β-Te displays positive Poisson's ratios (PPR) of 0.49 and 0.29 for uniaxial loading in the zigzag and armchair directions as shown in the ESI (Fig. S3).† The Poisson's ratio values for β-Te perfectly align with Gao *et al.*'s reported values.[48] However, there is a small deviation in the Poisson's ratio in the zigzag direction (0.58) calculated by Liu *et al.*[66]

The Poisson's ratio of the β′-Te monolayer is shown in Fig. 2(a) as a function of uniaxial deformation along the zigzag direction (*b*-axis) and Fig. 2(b) presents the Poisson's ratio for deformation along the armchair direction (*a*-axis). In Fig. 2(a), the data are fitted to the 7th order function, $y = -\nu_1 x + \nu_2 x^2 + \nu_3 x^3 + \nu_4 x^4 + \nu_5 x^5 + \nu_6 x^6 + \nu_7 x^7 + c$, which gives the linear Poisson's ratio $\nu_1 = 0.01$ and constant, $c = -5.21$. In Fig. 2(b), the calculated data are fitted to the function, $y = -\nu_1 x + \nu_2 x^2 + \nu_3 x^3 + \nu_4 x^4 + \nu_5 x^5 + c$. The linear Poisson's ratio obtained is $\nu_1 = 0.29$ and $c = -7.57$.

The ε_a *vs.* εb plot (Fig. 2(a)) shows that tellurene expands (or compressive strain decreases) in the *a*-axis when compressive strain along the *b*-axis is applied. This is referred to as positive Poisson's ratio. Tellurene also expands in the *a*-axis under applied tensile strain along the *b*-axis. When a material elongates in an axis upon stretching its other axis or *vice versa*, it is known as negative Poisson's ratio behavior. Therefore, uniaxial deformation in tellurene leads to positive Poisson's ratio upon applying negative strain and negative Poisson's ratio upon

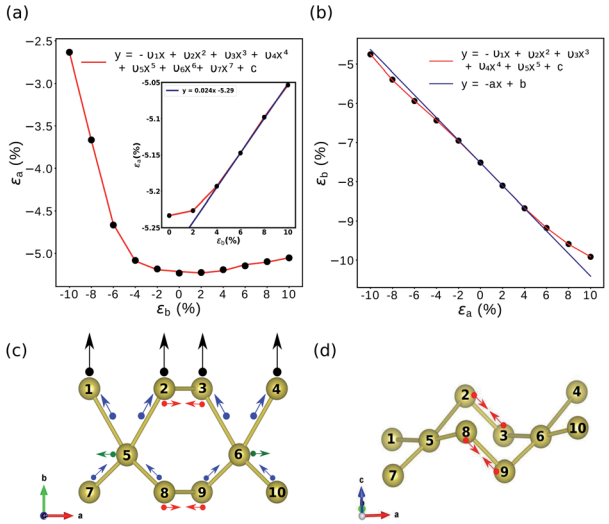

Fig. 2 Poisson's ratio as a function of uniaxial deformation of β′-Te: (a) εa *vs.* εb. The inset shows the NPR of tellurene under tensile strain. (b) εb *vs.* ε_a. (c) Top view and (d) side view of the NPR behavior of tellurene under a tensile strain of 10% in the zigzag direction (black arrows). The colored arrows represent the movement of atoms, with the blue ones representing the overall movement in the *b*-axis. The resulting tensile strain in the *a*-axis (green arrows) and compressive strain in the *c*-axis (red arrows) compensate for the applied strain. The size of the arrows represents the intensity of the stretch and compression.

applying positive strain. Materials exhibiting negative Poisson's ratio are called auxetic materials due to their unusual mechanical behaviour.[67] NPR in tellurene is attributed to the existence of a six-chair like arrangement of Te atoms in the puckered monolayer. The structural evolution for the in-plane NPR behavior is discussed in the ESI, Table S1.†

Quantitatively, a high PPR of 0.48 is obtained in the negative strain range which is close to the critical value, 0.5, for most of the materials.[5,68] For the applied positive strain, a linear negative Poisson's ratio equivalent to −0.024 is achieved. The linear NPR is quite small and this indicates that the tensile stress leads to a small lateral strain only. 1 T-MX_2 (M = Mo, W, Tc, Re; X = S, Se, Te) monolayers also display small in-plane negative Poisson's ratios ranging from −0.03 to −0.37.[67] Borophene also shows a NPR of −0.04 along *a* and −0.02 along *b*.[69] δ-phosphorene has a NPR of −0.267.[70] Black phosphorus exhibits a theoretical out-of-plane NPR of −0.027,[21] which has been experimentally validated.[71] Silica in its different 2D phases is reported to have a negative Poisson's ratio in the range of −0.02 to −0.12.[72] Other puckered 2D materials having a NPR include group V-enes (BP, As, and Sb) and group IV monochalcogenides (SiS, SiSe, GeS, GeSe, SnS, SnSe, and SnTe).[73]

Now, the effect of applied strain in the *a*-axis of β′-Te is observed on the *b*-axis (Fig. 2(b)). The application of strain in the armchair direction (*a*-axis) results in a strain in the zigzag direction (*b*-axis) in a way that only a positive Poisson's ratio is obtained for both the positive and negative applied strains. A linear positive Poisson's ratio of 0.29 is obtained from the εb *vs.* ε_a plot. β′-Te exhibits different Poisson's ratios for strain applied to the armchair and zigzag directions. This substantial anisotropy in the in-plane mechanical properties is related to the geometric anisotropy in the monolayer (Fig. 1(a)). The obtained PPR is comparable to that of 2D materials such as graphene ($\nu = 0.18$), BN ($\nu = 0.22$), BP ($\nu = 0.27$),[74] MoS_2 ($\nu = 0.30$),[4] ZrS_2 ($\nu = 0.19$), $ZrSe_2$ ($\nu = 0.20$), HfS_2 ($\nu = 0.18$) and $HfSe_2$ ($\nu = 0.21$).[5]

Mechanical strength of a nanomaterial can also be determined by its 2D elastic constants. The following conditions govern the mechanical stability of tellurene monolayers.[75]

$$C_{11}C_{22} - C_{12}^2 > 0 \text{ and } C_{11}, C_{22}, C_{66} > 0 \quad (1)$$

where C_{11}, C_{22}, C_{12} and C_{66} belong to the elastic tensor expressed as

$$C_{ij} = \begin{pmatrix} C_{11} & C_{12} & C_{13} & 0 & 0 & C_{16} \\ C_{12} & C_{22} & C_{23} & 0 & 0 & C_{26} \\ C_{13} & C_{23} & C_{33} & 0 & 0 & C_{36} \\ 0 & 0 & 0 & C_{44} & C_{45} & 0 \\ 0 & 0 & 0 & C_{45} & C_{55} & 0 \\ C_{16} & C_{26} & C_{36} & 0 & 0 & C_{66} \end{pmatrix} \quad (2)$$

The above conditions (eqn. (1)) are satisfied by both β-Te and β′-Te. By definition, elastic constant is $C_{ijkl} = \frac{d\sigma_{ij}}{d\varepsilon_{kl}}$, where σ_{ij} and ε_{kl} are the stress and strain tensors, respectively. In Voigt notation, the fourth order tensor has been reduced to the second order tensor as seen in eqn (2). For a highly stretchable material, elastic constants should be small and hence, it should have a small Young's modulus. This is preferable for easy displacement of the charges in 2D sheets to generate piezoelectricity. The anisotropic 2D Young's modulus for monoclinic tellurene is given by[66]

$$Y_{11} = \frac{C_{11}C_{22} - C_{12}^2}{C_{22}} \text{ and } Y_{22} = \frac{C_{11}C_{22} - C_{12}^2}{C_{11}} \quad (3)$$

Table 1 presents the elastic constants and Young's modulus of β-Te and β′-Te. The calculated elastic constants and Young's modulus of β-Te are close to the ones reported by Liu *et al.* at 0 K temperature.[66] Elastic constants C_{22} and C_{12} of β′-Te are smaller than the constants observed for β-Te. This implies that β′-Te is softer than β-Te in the *b*-direction whereas β-Te is more flexible in the *a*-direction. Also, the Young's modulus of β′-Te along the *b*-axis (Y_{22}) is much smaller than that along the *a*-axis (Y_{11}), indicating that β′-Te is softer in the zigzag direction. Tellurene is a low stiffness material as it has elastic constants and Young's modulus smaller than those of many 2D materials such as graphene ($C_{11} = 351.9$ N m^{-1}, $Y = 341$ N m^{-1}),[74] BN ($C_{11} = 290$ N m^{-1}, $Y = 275.9$ N m^{-1}),[74] BP ($C_{11} = 145$ N m^{-1}, $Y = 135.6$ N

Table 1 Elastic constants C_{11}, C_{22} and C_{12} and Young's modulus Y_{11} and Y_{22} of β-Te and β′-Te in units of N m^{-1}

Monolayer	C_{11}	C_{22}	C_{12}	Y_{11}	Y_{22}
β-Te	13.52	23.68	6.69	11.63	20.37
β′-Te	16.42	3.27	2.01	15.18	3.02

m^{-1}),[74] MoS_2 ($C_{11} = 134.9$ N m^{-1}, $Y = 125$ N m^{-1}),[4] $MoTe_2$ ($C_{11} = 88$ N m^{-1}, $Y = 79.9$ N m^{-1}),[9,76] ZrS_2 ($C_{11} = 75.57$ N m^{-1}, $Y = 72.55$ N m^{-1}), $ZrSe_2$ ($C_{11} = 68.86$ N m^{-1}, $Y = 65.83$ N m^{-1}), HfS_2 ($C_{11} = 80.77$ N m^{-1}, $Y = 77.99$ N m^{-1}) and $HfSe_2$ ($C_{11} = 75.07$ N m^{-1}, $Y = 71.85$ N m^{-1}).[5] Elastic constants of SnS, SnSe, GeS and GeSe[12] are also larger than those of tellurene.

Further, we have investigated the piezoelectric properties of β-Te and β′-Te. Also, the effect of strain is observed on their piezoelectric coefficients. The stress tensor is defined as

$$e_{ijk} = \frac{dP_i}{d\varepsilon_{jk}} \quad (4)$$

where P_i is the electrical polarization in the material as a result of the applied strain ε_{jk}. The subscripts i, j, and k refer to the spatial directions a, b and c (or 1, 2 and 3), respectively. VASP calculates the piezoelectric stress coefficient into two parts: electronic (e_{ijk}^{elec}) and ionic (e_{ijk}^{ion}) values as $e_{ijk} = e_{ijk}^{elec} + e_{ijk}^{ion}$. For different crystal lattices and symmetries, the number of independent elements of the tensor differs.[77] Therefore, the piezoelectric tensor of β′-Te (space group $P2$) following the Voigt notation (third order tensor reduced to second order) is

$$e_{ij} = \begin{pmatrix} 0 & 0 & 0 & e_{14} & e_{15} & 0 \\ e_{21} & e_{22} & e_{23} & 0 & 0 & e_{26} \\ 0 & 0 & 0 & e_{34} & e_{35} & 0 \end{pmatrix} \quad (5)$$

In two dimension, the number of independent elements reduces further due to increased symmetry. Therefore, elements e_{34} and e_{35} become zero. As the stress coefficients are evaluated directly using DFPT, the piezoelectric strain coefficients d_{ij} can be determined from the stress coefficients and elastic constants C_{ij} by the following relation,

$$e_{ik} = \sum_{j}^{6} d_{ij} C_{jk} \quad (6)$$

On solving the equations obtained from this relation (ESI†), the values of d_{ij} are obtained, which are experimentally relevant.

β-tellurene, being centrosymmetric, does not exhibit piezoelectricity. However, it shows piezoelectricity under the effect of strain. The phase transition to a $P2$ structure is obtained at 4.5% tensile biaxial strain resulting in high piezoelectric coefficients (Table 2). The complete variation of piezoelectricity under strain is shown in the ESI (Fig. S4†). Uniaxial strain has no effect on its inversion symmetry, thus leading to zero piezoelectricity. The piezoelectric stress coefficients of single layer non-centrosymmetric β′-tellurene have also been calculated and are tabulated in Table 2. It displays quite large coefficients than β-Te. Fig. 3(a)–(c) show the variation of all the elements of the stress tensor under the applied biaxial strain. Strain led to an enhancement in all the components of the piezoelectric tensor resulting in peaks for e_{21}, e_{22}, e_{23} and e_{26} at a compressive biaxial strain of −5.5% (Table 2). The shear strain components e_{14} and e_{15} increase with the increase in tensile strain. The highest element obtained is the in-plane polarization (e_{22}) having a value of -83.89×10^{-10} C m^{-1} ($d_{22} = -333.14$ pm V^{-1}). For all elements, the ionic contribution is higher than the electronic contribution, highlighting the ionic nature of bonds between Te atoms.

For uniaxial strain in the zigzag direction (Fig. 3(d)–(f)), the variation of piezoelectric coefficients is similar to the variation under biaxial strain although the magnitude is different. Again, in-plane polarization (-42.58×10^{-10} C m^{-1}) ($d_{22} = -302.22$ pm V^{-1}) is the highest for uniaxial deformation in the b-axis. Also, we observed a phase change from monoclinic $P2$ to $P2/m$ (denotes the centrosymmetry) below biaxial and uniaxial compressive strains −5.5% and −4.9%, respectively. We explore the variation in piezoelectric coefficients by deforming the structures under the application of uniaxial strain along the armchair direction also. However, it is observed that these structures attain the centrosymmetric nature in the whole range of −10% to +10% and hence, no piezoelectricity is obtained along the a-axis.

The in-plane piezoelectric coefficient of tellurene under biaxial and uniaxial strain in the zigzag direction is higher than that of MoS_2 by a factor of 23 and 12, respectively. This in-plane piezoelectric coefficient is remarkably huge and hence tellurene proves to be a great replacement for the existing traditional piezoelectric materials such as AlN (5.6 pm V^{-1}),[78] GaN (3.1 pm V^{-1}),[78] wurtzite-BN (0.60 pm V^{-1}), MoS_2 (3.73 pm V^{-1}) and quartz (2.3 pm V^{-1}).[1] The coefficients are found to be larger than the reported giant piezoelectricity in SnS (144.76 pm V^{-1}), SnSe (250.58 pm V^{-1}), GeS (75.43 pm V^{-1}), and GeSe (212.13).[12]

Table 2 Piezoelectric stress coefficients of β-Te and β′-Te under different strains in terms of ionic and electronic contributions. The units of e_{ij} and d_{ij} are 10^{-10} C m^{-1} and pm V^{-1}, respectively

		Ionic				Electronic				Net contribution				Net contribution			
Monolayer	Strain	e_{21}	e_{22}	e_{23}	e_{26}	e_{21}	e_{22}	e_{23}	e_{26}	e_{21}	e_{22}	e_{23}	e_{26}	d_{21}	d_{22}	d_{23}	d_{26}
β-Te	Biaxial strain (4.5%)	−3.88	−10.98	−0.90	0.29	1.36	−1.78	0.81	−0.52	−2.52	−12.76	−0.09	−0.23	36.69	−310.32	−15.18	−5.14
β′-Te	Strain (0%)	−3.12	−7.44	−0.78	0.31	1.35	−1.81	0.73	0.47	−1.77	−9.25	−0.05	0.78	25.79	−298.78	12.12	15.54
	Biaxial strain (−5.5%)	−36.68	−83.72	−3.81	−6.30	0.12	−0.17	0.13	−0.04	−36.56	−83.89	−3.68	−6.34	−106.94	−333.14	−95.15	−97.52
	Uniaxial strain along zigzag (−4.9%)	−17.79	−41.82	−1.25	−0.71	0.56	−0.76	0.59	−0.23	−17.23	−42.58	−0.66	−0.94	−112.48	−302.22	−30.37	−13.77

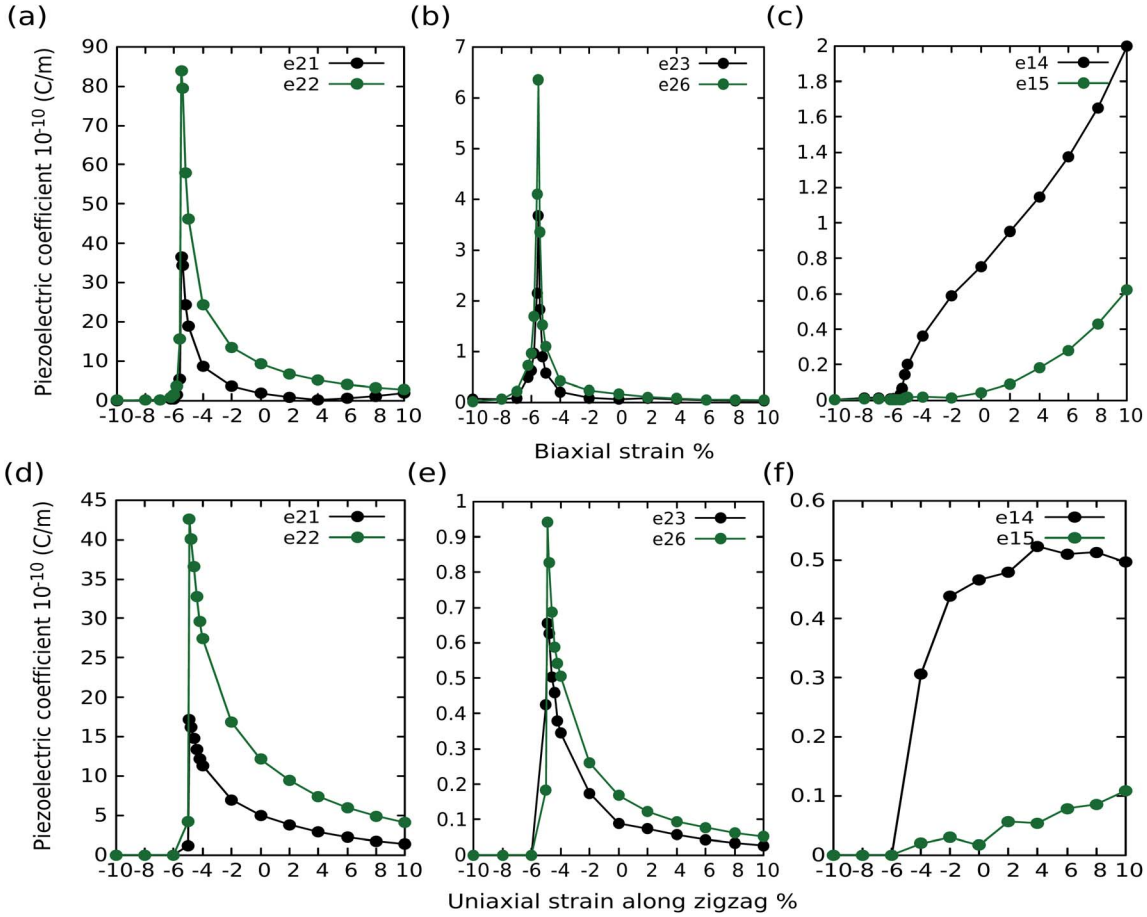

Fig. 3 Variation in piezoelectric stress coefficients of β′-Te as a function of (a)–(c) biaxial strain and (d)–(f) uniaxial strain along the zigzag direction. Variation of all six non-zero independent tensors is shown.

Spontaneous polarization is further analyzed using Born effective charges occurring in the 2D sheet. BEC (Z^*_{ij}) determine the change in polarization (P_i) caused by applied strain or the force (F_i) experienced by atoms due to the applied electric field (εj) as $Z^*_{ij} = \frac{\Omega}{e}\left(\frac{\partial P_i}{\partial u_j}\right) = \frac{1}{e}\left(\frac{\partial F_i}{\partial \varepsilon_j}\right)$, where Ω is the volume and u_j is the displacement in the system.

The diagonal dynamic charges on the β′-Te atoms are given in Table S2.† We find that for biaxial strain, charge on Te5 increases by 53% along the armchair direction and by 105% along the zigzag direction while Te2 and Te3 show a reduction in charges by the same amounts in the respective directions. Under a uniaxial strain of −4.9% in the zigzag direction, the increase and decrease of dynamic charges are nearly 48% and 93% for respective Te atoms. Dynamic charges developed along the *z*-direction are too small indicating no out-of-plane polarization. Typically, the materials having only one element are non-polar. But since Te exhibits multivalent nature and due to the different coordination of Te atoms (Fig. 1(a)) in this particular monolayer, there are different charges on the atoms. BECs indicate that Te5 acts as a donor while Te2 and Te3 atoms act as acceptors. Hence, the origin of the huge piezoelectricity is attributed to the relatively large BECs of Te atoms.

As the mechanical properties of tellurene ascertain that it is highly stretchable, it becomes important to determine the temperature dependent behavior of sheets. We calculated the thermal expansion of the Te monolayer using the quasi harmonic approximation. Both β and β′-Te are strained from −5% to +5% and phonon frequencies are calculated for all 11 structures. The equilibrium volume $V(T)$ is determined from the free energies $F(V, T)$ calculated at each temperature up to 400 K. The volume expansion and variation of coefficient of thermal expansion (α) with temperature are shown in Fig. 4. It is expressed as

$$\alpha = \frac{1}{V}\left(\frac{dV}{dT}\right)_p = \frac{1}{A}\left(\frac{dA}{dT}\right)_p \quad (7)$$

where A represents the in-plane area of the monolayer. It is observed that α is negative at low temperatures. The crossover temperatures for thermal contraction to thermal expansion are 32 K and 21 K for β and β′-Te, respectively.

Liu *et al.*[66] have shown anisotropic thermal expansion along the armchair and zigzag directions in β-Te where the negative expansion occurs particularly along the *a*-axis in the low temperature range. They have also observed large thermal expansion along the *b*-axis. We have obtained a similar thermal

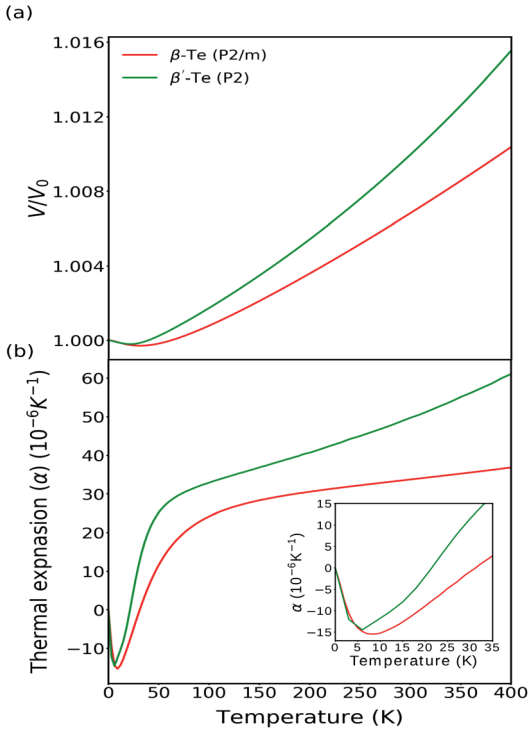

Fig. 4 Temperature dependence of (a) volume and (b) coefficient of thermal expansion of β and β′ tellurene.

expansion of β-Te lying in the same range. The thermal expansion attained in β′-Te is higher than that in β-Te. At low temperatures, the negative thermal expansion in β-Te and β′-Te is possibly because of the negative values of Grüneisen parameter.[66] Grüneisen parameter describes the change in vibrational properties with the change in volume. The variation of Grüneisen parameter with respect to temperature is shown in Fig. S6.†

In comparison to MoS_2,[32] tellurene is highly expandable and has thermal expansion higher by nearly 4 times for β-Te and 7 times for β′-Te at room temperature, 300 K. Also, expansion in tellurene is larger than in black phosphorene ($9 \sim 10 \times 10^{-6}$ K^{-1})[79] and $MoSe_2$ (8×10^{-6} K^{-1}).[30] Along with the large thermal expansion at room temperature, tellurene shows negative thermal expansion from 0 to 32 K. There are a few 2D materials that show negative thermal expansion in a broad range of temperature. This includes graphene,[30,31] doped graphene[31] and h-BN[30] exhibiting negative thermal expansion up to 1000 K and black phosphorene displaying negative expansion up to 150 K.[22] GeTe also falls into the category of materials having negative thermal expansion.[35]

4 Conclusion

In summary, we examined the mechanical and piezoelectric properties of tellurene under uniaxial and biaxial strains. The non-centrosymmetric β′-Te shows superior properties compared to the centrosymmetric β-Te monolayer. An in-plane negative Poisson's ratio of −0.024 is obtained under positive tensile strain in the zigzag direction of the β′-Te monolayer. The NPR behavior is due to the puckered structure of Te having a chair-like arrangement. The anisotropy in the geometric structure results in anisotropy in the mechanical and piezoelectric properties. The study reveals super-high piezoelectricity in the tellurene monolayer. The coefficients for tellurene are larger than the piezoelectricity observed in widely used MoS_2, that is, by a factor of 23 and 12 in the β′ phase under biaxial and uniaxial strain in the zigzag direction, respectively. Also, tellurene exhibits large thermal expansion, ∼4 times (β-Te) and ∼7 times (β′-Te) that of MoS_2 at 300 K with small thermal contraction at low temperatures. The gigantic piezoelectricity along with superior mechanical properties makes tellurene ideal for use in piezotronics.

Conflicts of interest

There are no conflicts to declare.

Acknowledgements

CB and PS appreciate the UGC for a JRF fellowship (Grant No. 3724/(NET-DEC2018)) as well as DST-SERB (Grant No. EEQ/2016/00049) for the financial support. CB is thankful to Jesús Carrete for helpful discussion and improving the phonon dispersion calculation.

References

1 K.-A. N. Duerloo, M. T. Ong and E. J. Reed, *J. Phys. Chem. Lett.*, 2012, **3**, 2871–2876.
2 M. N. Blonsky, H. L. Zhuang, A. K. Singh and R. G. Hennig, *ACS Nano*, 2015, **9**, 9885–9891.
3 M. M. Alyörük, Y. Aierken, D. Çakır, F. M. Peeters and C. Sevik, *J. Phys. Chem. C*, 2015, **119**, 23231–23237.
4 N. Jena, S. D. Behere and A. De Sarkar, *J. Phys. Chem. C*, 2017, **121**, 9181–9190.
5 N. Jena, A. Rawat, R. Ahammed, M. K. Mohanta, A. De Sarkar, *et al.*, *J. Mater. Chem. A*, 2018, **6**, 24885–24898.
6 R. Hinchet, U. Khan, C. Falconi and S.-W. Kim, *Mater. Today*, 2018, **21**, 611–630.
7 W. Wu, L. Wang, Y. Li, F. Zhang, L. Lin, S. Niu, D. Chenet, X. Zhang, Y. Hao, T. F. Heinz, *et al.*, *Nature*, 2014, **514**, 470–474.
8 H. Zhu, Y. Wang, J. Xiao, M. Liu, S. Xiong, Z. J. Wong, Z. Ye, Y. Ye, X. Yin and X. Zhang, *Nat. Nanotechnol.*, 2015, **10**, 151–155.
9 M. Yagmurcukardes, C. Sevik and F. Peeters, *Phys. Rev. B*, 2019, **100**, 045415.
10 L. Dong, J. Lou and V. B. Shenoy, *ACS Nano*, 2017, **11**, 8242–8248.
11 W. Li and J. Li, *Nano Res.*, 2015, **8**, 3796–3802.
12 R. Fei, W. Li, J. Li and L. Yang, *Appl. Phys. Lett.*, 2015, **107**, 173104.
13 L. C. Gomes, A. Carvalho and A. H. Castro Neto, *Phys. Rev. B*, 2015, **92**, 214103.

14 J. Tan, Y. Wang, Z. Wang, X. He, Y. Liu, B. Wang, M. I. Katsnelson and S. Yuan, *Nano Energy*, 2019, **65**, 104058.
15 L. Zhang, C. Tang, C. Zhang and A. Du, *Nanoscale*, 2020, **12**, 21291–21298.
16 W. Ma, J. Lu, B. Wan, D. Peng, Q. Xu, G. Hu, Y. Peng, C. Pan and Z. L. Wang, *Adv. Mater.*, 2020, **32**, 1905795.
17 L. Drissi, S. Sadki and K. Sadki, *J. Phys. Chem. Solids*, 2018, **112**, 137–142.
18 A. Apte, S. Kouser, F. S. Samghabadi, L. Chang, L. M. Sassi, D. Litvinov, B. I. Yakobson, A. B. Puthirath and P. M. Ajayan, *Mater. Today*, 2020, in press.
19 S. Gao, Y. Wang, R. Wang and W. Wu, *Semicond. Sci. Technol.*, 2017, **32**, 104004.
20 Z. Qin, G. Qin and M. Hu, *Nanoscale*, 2018, **10**, 10365–10370.
21 J.-W. Jiang and H. S. Park, *Nat. Commun.*, 2014, **5**, 1–7.
22 L. Wang, C. Wang and Y. Chen, *J. Phys.: Condens. Matter*, 2019, **31**, 465003.
23 G. Qin and Z. Qin, *npj Comput. Mater.*, 2020, **6**, 1–6.
24 X. Li, C. Huang, S. Hu, B. Deng, Z. Chen, W. Han and L. Chen, *J. Mater. Chem. C*, 2020, **8**, 4021–4029.
25 N. R. Keskar and J. R. Chelikowsky, *Nature*, 1992, **358**, 222–224.
26 D. T. Ho, S.-D. Park, S.-Y. Kwon, K. Park and S. Y. Kim, *Nat. Commun.*, 2014, **5**, 1–8.
27 K. Wojciechowski, *Phys. Lett. A*, 1989, **137**, 60–64.
28 D. Prall and R. Lakes, *Int. J. Mech. Sci.*, 1997, **39**, 305–314.
29 C. Huang and L. Chen, *Adv. Mater.*, 2016, **28**, 8079–8096.
30 C. Sevik, *Phys. Rev. B: Condens. Matter Mater. Phys.*, 2014, **89**, 035422.
31 S. Mann, R. Kumar and V. Jindal, *RSC Adv.*, 2017, **7**, 22378–22387.
32 L. F. Huang, P. L. Gong and Z. Zeng, *Phys. Rev. B: Condens. Matter Mater. Phys.*, 2014, **90**, 045409.
33 Y. Ge, Z. Ding, W. Meng, J. Wang, Y. Hou, G. Wu, Q. Lu and X. Yang, *Phys. Rev. B*, 2020, **101**, 104305.
34 Y. Ding and B. Xiao, *RSC Adv.*, 2015, **5**, 18391–18400.
35 Đ. Dangić, A. R. Murphy, É. D. Murray, S. Fahy and I. Savić, *Phys. Rev. B*, 2018, **97**, 224106.
36 H. Sun, G. Liu, Q. Li and X. Wan, *Phys. Lett. A*, 2016, **380**, 2098–2104.
37 K. S. Novoselov, A. K. Geim, S. V. Morozov, D. Jiang, Y. Zhang, S. V. Dubonos, I. V. Grigorieva and A. A. Firsov, *science*, 2004, **306**, 666–669.
38 J. Chen, Y. Dai, Y. Ma, X. Dai, W. Ho and M. Xie, *Nanoscale*, 2017, **9**, 15945–15948.
39 W. Wu, G. Qiu, Y. Wang, R. Wang and P. Ye, *Chem. Soc. Rev.*, 2018, **47**, 7203–7212.
40 D. Zhou, H. Li, N. Si, H. Li, H. Fuchs and T. Niu, *Adv. Funct. Mater.*, 2020, 2006997.
41 Z. Shi, R. Cao, K. Khan, A. K. Tareen, X. Liu, W. Liang, Y. Zhang, C. Ma, Z. Guo, X. Luo, *et al.*, *Nano-Micro Lett.*, 2020, **12**, 1–34.
42 A. K. Tareen, K. Khan, M. Aslam, H. Zhang and X. Liu, *Nanoscale*, 2021, **13**, 510–552.
43 X. Cai, X. Han, C. Zhao, C. Niu and Y. Jia, *J. Semicond.*, 2020, **41**, 081002.
44 Y. Wang, G. Qiu, R. Wang, S. Huang, Q. Wang, Y. Liu, Y. Du, W. A. Goddard, M. J. Kim, X. Xu, *et al.*, *Nat. Electron.*, 2018, **1**, 228–236.
45 L. Ramírez-Montes, W. López-Pérez, R. González-Hernández and C. Pinilla, *Int. J. Quantum Chem.*, 2020, e26267.
46 S. Huang, M. Segovia, X. Yang, Y. R. Koh, Y. Wang, D. Y. Peide, W. Wu, A. Shakouri, X. Ruan and X. Xu, *2D Materials*, 2019, **7**, 015008.
47 D. K. Sang, T. Ding, M. N. Wu, Y. Li, J. Li, F. Liu, Z. Guo, H. Zhang and H. Xie, *Nanoscale*, 2019, **11**, 18116–18123.
48 Z. Gao, F. Tao and J. Ren, *Nanoscale*, 2018, **10**, 12997–13003.
49 Z. Gao, G. Liu and J. Ren, *ACS Appl. Mater. Interfaces*, 2018, **10**, 40702–40709.
50 Z. Zhu, X. Cai, S. Yi, J. Chen, Y. Dai, C. Niu, Z. Guo, M. Xie, F. Liu, J.-H. Cho, *et al.*, *Phys. Rev. Lett.*, 2017, **119**, 106101.
51 D. Wines, J. A. Kropp, G. Chaney, F. Ersan and C. Ataca, *Phys. Chem. Chem. Phys.*, 2020, **22**, 6727–6737.
52 D. K. Sang, B. Wen, S. Gao, Y. Zeng, F. Meng, Z. Guo and H. Zhang, *Nanomaterials*, 2019, **9**, 1075.
53 Y. Wang, C. Xiao, M. Chen, C. Hua, J. Zou, C. Wu, J. Jiang, S. A. Yang, Y. Lu and W. Ji, *Mater. Horiz.*, 2018, **5**, 521–528.
54 X. Cai, Y. Ren, M. Wu, D. Xu and X. Luo, *Nanoscale*, 2020, **12**, 167–172.
55 G. Kresse and J. Furthmüller, *Comput. Mater. Sci.*, 1996, **6**, 15–50.
56 P. E. Blöchl, *Phys. Rev. B: Condens. Matter Mater. Phys.*, 1994, **50**, 17953.
57 G. Kresse and D. Joubert, *Phys. Rev. B: Condens. Matter Mater. Phys.*, 1999, **59**, 1758.
58 J. P. Perdew, K. Burke and M. Ernzerhof, *Phys. Rev. Lett.*, 1996, **77**, 3865.
59 M. Ernzerhof and G. E. Scuseria, *J. Chem. Phys.*, 1999, **110**, 5029–5036.
60 S. Baroni, S. De Gironcoli, A. Dal Corso and P. Giannozzi, *Rev. Mod. Phys.*, 2001, **73**, 515.
61 X. Wu, D. Vanderbilt and D. Hamann, *Phys. Rev. B: Condens. Matter Mater. Phys.*, 2005, **72**, 035105.
62 Y. Le Page and P. Saxe, *Phys. Rev. B: Condens. Matter Mater. Phys.*, 2002, **65**, 104104.
63 A. Togo, L. Chaput, I. Tanaka and G. Hug, *Phys. Rev. B: Condens. Matter Mater. Phys.*, 2010, **81**, 174301.
64 A. Togo and I. Tanaka, *Scr. Mater.*, 2015, **108**, 1–5.
65 H. Ma, W. Hu and J. Yang, *Nanoscale*, 2019, **11**, 21775–21781.
66 G. Liu, Z. Gao and J. Ren, *Phys. Rev. B*, 2019, **99**, 195436.
67 L. Yu, Q. Yan and A. Ruzsinszky, *Nat. Commun.*, 2017, **8**, 1–8.
68 T. Jing, D. Liang, M. Deng and S. Cai, *J. Mater. Chem. C*, 2020, **8**, 10382–10389.
69 A. J. Mannix, X.-F. Zhou, B. Kiraly, J. D. Wood, D. Alducin, B. D. Myers, X. Liu, B. L. Fisher, U. Santiago, J. R. Guest, *et al.*, *Science*, 2015, **350**, 1513–1516.
70 H. Wang, X. Li, P. Li and J. Yang, *Nanoscale*, 2017, **9**, 850–855.
71 Y. Du, J. Maassen, W. Wu, Z. Luo, X. Xu and P. D. Ye, *Nano Lett.*, 2016, **16**, 6701–6708.
72 Z. Gao, X. Dong, N. Li and J. Ren, *Nano Lett.*, 2017, **17**, 772–777.
73 B. Liu, M. Niu, J. Fu, Z. Xi, M. Lei and R. Quhe, *Phys. Rev. Mater.*, 2019, **3**, 054002.

74 D. Çakır, D. Kecik, H. Sahin, E. Durgun and F. M. Peeters, *Phys. Chem. Chem. Phys.*, 2015, **17**, 13013–13020.
75 Y. Dong, B. Zeng, X. Zhang, D. Li, J. He and M. Long, *J. Appl. Phys.*, 2019, **125**, 064304.
76 Z. Fan, Z. Wei-Bing and T. Bi-Yu, *Chin. Phys. B*, 2015, **24**, 097103.
77 M. De Jong, W. Chen, H. Geerlings, M. Asta and K. A. Persson, *Sci. Data*, 2015, **2**, 1–13.
78 C. Lueng, H. L. Chan, C. Surya and C. Choy, *J. Appl. Phys.*, 2000, **88**, 5360–5363.
79 Y. Aierken, D. Çakır, C. Sevik and F. M. Peeters, *Phys. Rev. B: Condens. Matter Mater. Phys.*, 2015, **92**, 081408.